The Astrophysical Journal, 974:162 (13pp), 2024 October 20 https://doi.org/10.3847/1538-4357/ad6c50

Structured Jet Model for Multiwavelength Observations of the Jetted Tidal Disruption Event AT 2022cmc

Chengchao Yuan (袁成超)[1], B. Theodore Zhang (张兵)[2], Walter Winter[1], and Kohta Murase[2,3]

[1] Deutsches Elektronen-Synchrotron DESY, Platanenallee 6, 15738 Zeuthen, Germany; chengchao.yuan@desy.de

[2] Center for Gravitational Physics and Quantum Information, Yukawa Institute for Theoretical Physics, Kyoto University, Kyoto 606-8502, Japan

[3] Department of Physics, Department of Astronomy & Astrophysics, Center for Multimessenger Astrophysics, Institute for Gravitation and the Cosmos, The Pennsylvania State University, University Park, PA 16802, USA

Received 2024 June 19; revised 2024 August 1; accepted 2024 August 5; published 2024 October 10

Abstract

AT 2022cmc is a recently documented tidal disruption event that exhibits a luminous jet, accompanied by fast-declining X-ray and long-lasting radio and millimeter emission. Motivated by the distinct spectral and temporal signatures between the X-ray and radio observations, we propose a multizone model involving relativistic jets with different Lorentz factors. We systematically study the evolution of faster and slower jets in an external density profile, considering the continuous energy injection rate associated with time-dependent accretion rates before and after the mass fallback time. We investigate time-dependent multiwavelength emission from both the forward shock (FS) and reverse shock (RS) regions of the fast and slow jets, in a self-consistent manner. Our analysis demonstrates that the energy injection rate can significantly impact the jet evolution and subsequently influence the lightcurves. We find that the X-ray spectra and lightcurves could be described by electron synchrotron emission from the RS of the faster jet, in which the late-time X-ray upper limits, extending to 400 days after the disruption, could be interpreted as a jet break. Meanwhile, the radio observations can be interpreted as a result of synchrotron emission from the FS region of the slower jet. We also discuss prospects for testing the model with current and future observations.

Unified Astronomy Thesaurus concepts: Tidal disruption (1696); Transient sources (1851); Radiative processes (2055); Relativistic jets (1390)

1. Introduction

Tidal disruption events (TDEs) are astronomical phenomena that occur when a star is torn apart by the gravitational forces of a supermassive black hole (SMBH) as the star orbits in close proximity to the SMBH (e.g., Hills 1975; Rees 1988; Evans & Kochanek 1989). The subsequent accretion activities, fueled by the bound mass of the star, can generate a luminous transient spanning a broad electromagnetic spectrum, including the radio, optical, ultraviolet, X-ray, and γ-ray bands. Among the expanding catalog of recorded TDEs, four TDEs, including Swift J1644+57 (Bloom et al. 2011; Burrows et al. 2011), Swift J2058+05 (Cenko et al. 2012), Swift J1112-8238 (Brown et al. 2015), and AT 2022cmc (Andreoni et al. 2022), have been classified as jetted TDEs. These jetted TDEs display prominent signatures of relativistic outflows, including fast-decaying lightcurves and nonthermal flux intensities in X-ray bands, alongside bright, long-lived radio emission (e.g., Pasham et al. 2023; Yao et al. 2024).

It has been thought that the radio emission is explained by synchrotron emission of electrons accelerated at external forward shocks (FSs; e.g., Giannios & Metzger 2011; Zauderer et al. 2011; Berger et al. 2012; Metzger et al. 2012; Zauderer et al. 2013; Eftekhari et al. 2018; Cendes et al. 2021; Matsumoto & Metzger 2023) as the jet propagates into the circumnuclear medium and becomes decelerated, resembling the physics of γ-ray burst (GRB) afterglows (e.g., Zhang 2018).

As for X-ray emission from jetted TDEs, interpreting them within the same emission zone for the radio emission is challenging. Different sites or mechanisms—such as magnetically dominated jets (Burrows et al. 2011), variable accretion near the SMBH horizon (Reis et al. 2012), and inverse Compton scattering of external photons (Bloom et al. 2011; Crumley et al. 2016)—are proposed to describe the X-ray observations. A self-consistent physical framework is needed to interpret the multiwavelength spectral energy distributions (SEDs) and the temporal evolutions of the radio and X-ray emission.

The recent documented jetted TDE AT 2022cmc at redshift $z = 1.19$ provides us with another prototype for multiwavelength modeling. AT 2022cmc was discovered by the Zwicky Transient Facility in the optical band (Andreoni et al. 2022). The short variability timescale in the SMBH rest frame, $t_{\rm var} \lesssim 1000\ {\rm s}/(1+z)$, implies an upper limit of the SMBH mass of a few $\times 10^7\ M_\odot$ (Yao et al. 2024). A relativistic jet with a high Lorentz factor ~ 100 was initially suggested to explain its superluminous and fast evolving X-ray (e.g., $L_X \propto t^{-2}$) and long-lasting radio emissions (Pasham et al. 2023). Moreover, an equipartition analysis (e.g., Chevalier 1998; Barniol Duran et al. 2013) and a detailed afterglow model revealed the radio- and millimeter-emitting plasma to be expanding relativistically (Matsumoto & Metzger 2023; Yao et al. 2024), e.g., $\Gamma \lesssim 2-5$. A two-component jet model with a fast inner component and slow outer component has also been exploited to explain the multiwavelength emission from TDEs (Wang et al. 2014; Liu et al. 2015; Mimica et al. 2015; Teboul & Metzger 2023; Sato et al. 2024). Recently, Zhou et al. (2024) demonstrated that the early and late radio emission of AT 2022cmc can be described by the FSs of fast and slow jets but in the best-fitting cases, the model is insufficient to reproduce the X-ray lightcurves, which implies that the radio, millimeter, and X-ray emission may have different origins.

Motivated by the distinct signatures between the radio, millimeter, and X-ray signals, such as their lightcurves (e.g., long-lasting versus fast decaying), their variability timescales (e.g., day timescale; Rhodes et al. 2023; versus $\sim 10^3$ s), and their spectral shapes (e.g., synchrotron self-absorption (SSA) tail versus synchrotron broken power law), we present a multizone model incorporating a fast relativistic jet (narrow outflow, denoted as a "fast jet") and a slow relativistic jet (wide outflow, denoted as a "slow jet") capable of explaining the X-ray and radio SEDs and lightcurves simultaneously. Each jet has a top-hat structure and points toward the observer. In addition to TDEs, structured jets have been extensively studied in the context of GRBs for a long time (e.g., Rossi et al. 2002; Zhang & Mészáros 2002; Sato et al. 2021; Zhang et al. 2023).

In this work, following the treatment for GRB blast waves (Nava et al. 2013; Zhang 2018; Zhang et al. 2023), we solve the differential equations governing the time evolution of jets sweeping an external medium, taking into account the time-dependent continuous energy and mass injections. We then compute the time-dependent synchrotron and inverse Compton emission from the FS and reverse shock (RS) regions. Our results demonstrate that the radio and millimeter observations can be explained by the FS model of the slow jet, and the fast jet RS synchrotron emissions can reproduce the X-ray spectra and lightcurve. We also argue that the steepening of the late-time (approximately 200−400 days after disruption) X-ray lightcurve, as reported in Eftekhari et al. (2024), could be attributed to a jet break as the jet Lorentz factor decreases.

The paper is organized as follows. In Section 2, we model the accretion history. The physical picture and time evolution of jets are presented in Section 3. We then apply the dynamics of jets to compute the time-dependent synchrotron and inverse Compton emissions in the jet FS and RS regions of the fast and slow jets in Section 4, where the radio, millimeter, and X-ray SEDs in three epochs (15–16 days, 25–27 days, and 41–46 days in the observer frame) and lightcurves extending to 400 days after the disruption are also fitted. A discussion and a summary are given in Section 5 and Section 6, respectively.

Throughout the paper, we use T, t, and t' to denote the times measured in the observer frame, SMBH rest frame, and jet comoving frame, respectively. The subscripts "f" and "s" will be used to denote the quantities related to fast and slow jets. The notation Q_x represents $Q/10^x$ in cgs units unless otherwise specified.

2. Accretion Rate onto a Supermassive Black Hole

Considering the disruption of a star of mass $M_\star$ and radius $R_\star$ by a SMBH of mass $M_{\rm BH}$, we estimate the tidal radius to be $R_T \approx f_T\,(M_{\rm BH}/M_\star)^{1/3} R_\star$ (e.g., Rees 1988), where $f_T \sim 0.02$–0.3, accounting for corrections from the stellar internal density profile (e.g., Phinney 1989; Piran et al. 2015). For a main-sequence star, the radius can be related to the mass via $R_\star = R_\odot (M_\star/M_\odot)^{1-\xi}$, where $R_\odot$ and $M_\odot$ are the solar radius and mass, respectively, and the parameter $\xi \sim 0.4$ for $1 < M_\star/M_\odot < 10$ (Kippenhahn & Weigert 1990). Based on the rather loose constraints on the SMBH mass of AT 2022cmc, e.g., $M_{\rm BH} < 5 \times 10^8\ M_\odot$ (Andreoni et al. 2022), and the upper limit obtained from the X-ray variability, e.g., $M_{\rm BH} < 5 \times 10^7\ M_\odot$ (Yao et al. 2024), we select $M_{\rm BH} = 10^7\ M_{\rm BH,7}\ M_\odot$ and $M_\star = 5\ M_{\star,0.7}\ M_\odot$ as fiducial parameters[4]. and obtain the corresponding tidal radius $R_T \simeq 1.2 \times 10^{13}$ cm. After undergoing tidal disruption, approximately half of the stellar material may persist in a gravitationally bound state within an eccentric orbit, ultimately leading to its return and potential accretion onto the SMBH. The fallback time can be estimated using the orbital period of the most tightly bound matter, expressed explicitly as $t_{\rm fb} \approx 2\pi\sqrt{a_{\rm min}^3/GM_{\rm BH}}$, where $a_{\rm min} \approx R_T^2/(2R_\star)$ is the semimajor axis of the orbit. In our fiducial case, we have $t_{\rm fb} \simeq 3.3 \times 10^6\ {\rm s}\, f_{T,-1.2}^{1/2} M_{\rm BH,7}^{1/2} M_{\star,0.7}^{-1/10}$.

The mass fallback could result in the formation of an accretion disk, with the accretion rate onto the SMBH following a $t^{-5/3}$ proportionality law after the fallback time. Here, t denotes the time measured in the rest frame of the SMBH, which can be correlated with the observation time, $T_{\rm obs}$, through $t = T_{\rm obs}/(1+z)$. Accretion may also occur prior to $t_{\rm fb}$. In this study, for the general purposes, we presume a power-law decay of the accretion rate before the fallback of the most tightly bound material and explicitly express the time-dependent accretion rates before and after $t_{\rm fb}$ as

$$\dot{M}_{\rm BH} = \frac{\eta_{\rm acc} M_\star}{\mathcal{C} t_{\rm fb}} \times \begin{cases} \left(\dfrac{t}{t_{\rm fb}}\right)^{-\alpha}, & t < t_{\rm fb}, \\ \left(\dfrac{t}{t_{\rm fb}}\right)^{-5/3}, & t > t_{\rm fb}, \end{cases} \tag{1}$$

where $0 \leqslant \alpha < 1$ is the free early time accretion index[5], the accretion efficiency $\eta_{\rm acc}$ represents the fraction of bounded materials that eventually ends up being accreted to the SMBH, and $\mathcal{C} \equiv 3 + 2/(1-\alpha)$ is introduced to normalize the total accreted mass, e.g., $\int \dot{M}_{\rm BH} dt = \eta_{\rm acc} M_\star/2$. The accretion efficiency, $\eta_{\rm acc}$, typically depends on the dynamics of mass fallback and disk formation, since typically a fraction of mass would fallback and end up forming a disk. Nevertheless, for simplicity, we opt for a constant value of $\eta_{\rm acc} = 0.1$ (e.g., Murase et al. 2020), noting its degeneracy with other parameters. Hence, the accretion rate at $t_{\rm fb}$ can be explicitly written as

$$\dot{M}_{\rm BH}(t_{\rm fb}) c^2 \simeq 5.5 \times 10^{46}\ {\rm erg\ s^{-1}}\, \eta_{\rm acc,-1} \mathcal{C}_{0.7} \times f_{T,-1.2}^{-1/2} M_{\rm BH,7}^{-1/2} M_{\star,0.7}^{1.1}, \tag{2}$$

which implies the accretion rate is initially in the super-Eddington regime, e.g., $\dot{M}_{\rm BH} c^2 \gtrsim L_{\rm Edd}/\eta_{\rm rad} \simeq 1.26 \times 10^{46} M_{\rm BH,7} \eta_{\rm rad,-1}^{-1}$ erg s^{-1}, where $L_{\rm Edd}$ is the Eddington luminosity and $\eta_{\rm rad} \sim 0.1$ is the radiation efficiency.

3. Jet Dynamics

In this section, we describe the physical framework of our structured jet model and derive the time evolution of the jet Lorentz factors incorporating continuous energy and mass

---

[4] The value of $M_\star$ is degenerate with the energy conversion efficiencies and will be justified in Section 5

[5] Shen & Matzner (2014) pointed out that a slow-decaying accretion rate is possible due to the disk's internal kinematic viscosity, depending on the type of polytrope star.

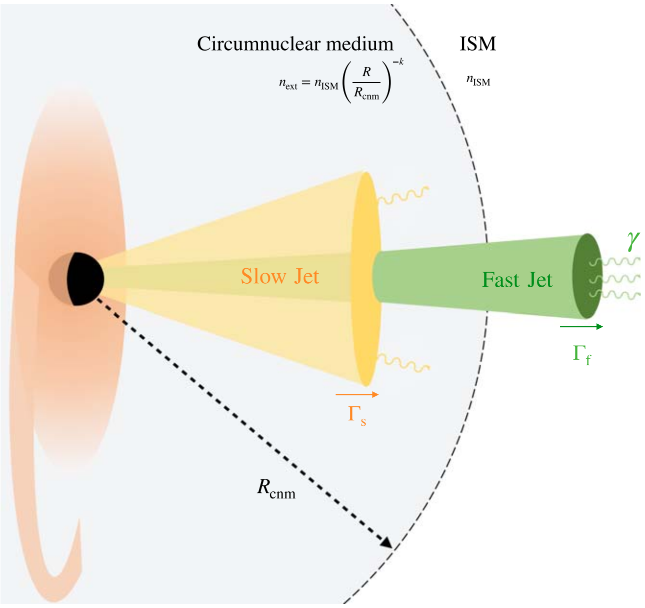

Figure 1. A schematic picture of the structured jet model. A slow jet propagating with Lorentz factor $\Gamma_{\rm s}$ in the circumnuclear material edge ($R_{\rm s} < R_{\rm cnm}$) and a fast jet with Lorentz factor $\Gamma_{\rm f}$ propagating in an ISM ($R_{\rm f} > R_{\rm cnm}$) are illustrated.

injections. These derivations will be used in Section 4 to compute the time-dependent electromagnetic emissions.

3.1. The Physical Picture

Multiwavelength follow-ups of AT 2022cmc demonstrate distinct signatures between its radio, optical, and X-ray emissions, which imply that they may originate from different radiation zones.

First, regarding the SEDs, we find that the radio spectra align with SSA tails in the electron slow-cooling regime. The optical spectra exhibit good agreement with blackbody distributions whereas the X-ray spectra are consistent with either a single power-law or a broken power-law distribution predicted by synchrotron radiation (Pasham et al. 2023; Yao et al. 2024). In this case, these emissions likely stem from different physical environments characterized by distinct compactness and magnetic fields. For example, the radio and X-ray emissions may be generated by nonthermal electrons accelerated in extended shocks, while the thermal optical emissions probably originate from a thermal envelope within the accretion disk or a hot corona.

Second, concerning the temporal evolution, the radio signals display a long-lasting lightcurve, contrasting with the rapidly decaying X-ray lightcurves, which implies that these emissions might be produced in different regions governed by disparate kinetic equations and initial conditions. A relativistic jet with a Lorentz factor greater than 10 is suggested to explain the bright and hard X-ray emissions. Zhou et al. (2024) also demonstrated that a single wide, slow jet similar to GRB afterglow models is insufficient to reproduce the radio and X-ray observations simultaneously.

Motivated by these considerations, we consider a time-dependent structured jet model, where the fast, narrow jet and the slow, wide jet are respectively adopted to explain the X-ray and radio lightcurves and spectra at various epochs. Figure 1 illustrates the configuration of our multizone model, depicting an accretion disk, a fast jet with Lorentz factor $\Gamma_{\rm f}$, and a slow jet with Lorentz factor $\Gamma_{\rm s}$. As for the density profile of the external medium, we connect a circumnuclear material edge within the radius $R_{\rm cnm}$ to the interstellar medium (ISM). We explicitly write down the density profile (in units of cm^{-3}) in terms of the distance (R) to the SMBH,

$$n_{\rm ext}(R) = \begin{cases} n_{\rm ISM}\left(\dfrac{R}{R_{\rm cnm}}\right)^{-k}, & R < R_{\rm cnm}, \\ n_{\rm ISM}, & R > R_{\rm cnm}, \end{cases} \tag{3}$$

where $n_{\rm ISM}$ is the number density of ISM and $1.5 \leqslant k \leqslant 2$ is the index of the density profile within the material edge radius $R_{\rm cnm}$ as suggested by radio data fitting (e.g., Matsumoto & Metzger 2023; Yao et al. 2024; Zhou et al. 2024). One potential source of the circumnuclear material is the wind emanating from preexisting disks. In this scenario, the circumnuclear material radius could extend to $R_{\rm cnm} \sim 10^{18}$ cm before merging with the ISM (Yuan et al. 2020, 2021). In the subsequent subsections, we adopt $k = 1.8$ and $R_{\rm cnm} = 10^{18}$ cm as fiducial parameters and model the dynamics of jets using $n_{\rm ext}$ defined in Equation (3). We will demonstrate in the following subsections that within the data-fitting time window, the fast and slow jets propagate, respectively, in the ISM (e.g., $R_{\rm f} > R_{\rm cnm}$) and the circumnuclear material (e.g., $R_{\rm s} < R_{\rm cnm}$).

Before delving into the kinetic equations for the jets, let us first parameterize the power converted to the fast and slow outflows from accretion using the energy conversion efficiencies $\eta_{\rm f}$ and $\eta_{\rm s}$,

$$L_{\rm f/s} = \eta_{\rm f/s}\dot{M}_{\rm BH}c^2, \tag{4}$$

where $\eta_{\rm f/s} \sim \mathcal{O}(0.1 - 1)$ represents the fraction of the accreted power is converted to jet.

3.2. Jet Evolution with Continuous Energy Injection

We follow the methodology for blast-wave dynamics, as in the diagram of GRB afterglow modeling (Nava et al. 2013; Zhang 2018; Zhang et al. 2023), to derive the differential equations governing the evolution of the jet, incorporating time-dependent energy and mass injections. For the fast jet initial Lorentz factor $\Gamma_{\rm f0} \sim \mathcal{O}(10)$ to be used in the multiwavelength modeling, we estimate the early time fast jet radius in the order of

$$R_{\rm f} \sim \frac{2\Gamma_{\rm f0}^2 c T_{\rm obs}}{1+z} \simeq 2.1 \times 10^{18}\ {\rm cm}\left(\frac{\Gamma_{\rm f0}}{30}\right)^2\left(\frac{T_{\rm obs}}{1\ {\rm day}}\right), \tag{5}$$

which is larger than $R_{\rm cnm}$ and implies the fast jet is propagating inside the ISM in the time window for lightcurve and SED fitting, e.g., $T_{\rm obs} \gtrsim 10$ days. We will show later in this section that the slow jet with initial Lorentz factor $\Gamma_{\rm s0} \sim 5$ will decelerate inside the circumnuclear material for $T_{\rm obs} \lesssim 100$ days. For both jets, we ignore adiabatic cooling of the jet as it becomes important only when a density profile index $k \geqslant 3$ is used (see Nava et al. 2013; Zhang 2018, for details).

Let us consider a general case where a jet of initial Lorentz factor Γ_0 penetrates deeply into an ambient gaseous medium. The jet sweeps up material, resulting in the formation of an FS that accelerates the upstream ISM to Lorentz factor $\Gamma \lesssim \Gamma_0$, and an RS that decelerates unshocked ejecta from an initial Lorentz factor Γ_0 to Γ. Figure 5 schematically shows the geometry of the FS, RS, and the discontinuity between their downstreams. We consider a simplified case that neglects the impact of the RS on jet evolution. A comprehensive treatment incorporating the RS and a justification for this simplification is provided in Appendix A.

We utilize the fast jet as an exemplar to derive the differential equations describing the jet's evolution. Adopting the approach used in external shock models for GRB afterglow modeling (e.g., Huang et al. 1999; Pe'er 2012; Nava et al. 2013) and neglecting radiative cooling, we express the total isotropic-equivalent energy of the relativistic jet as

$$\mathcal{E}_{\rm f,iso} = \Gamma_{\rm f} M_{\rm ej} c^2 + \Gamma_{\rm f} m_{\rm ext} c^2 + \Gamma_{\rm f,eff} \mathcal{E}'_{\rm f,int}, \tag{6}$$

where $M_{\rm ej}$ represents the isotropic-equivalent ejecta mass, $m_{\rm ext}$ is the external mass swept by the outflow, $\mathcal{E}'_{\rm f,int} = (\Gamma_{\rm f} - 1) m_{\rm ext} c^2$ represents the internal energy of the shocked material (downstream) in the jet comoving frame, $\Gamma_{\rm f,eff} = (\hat{\gamma}\Gamma_{\rm f}^2 - \hat{\gamma} + 1)/\Gamma_{\rm f}$ is the effective Lorentz factor, and $\hat{\gamma} = (4 + \Gamma_{\rm f}^{-1})/3$ is an adiabatic index taking into account the transition from relativistic to mildly relativistic. Noting the continuous energy and mass injections and the propagation of the outflow, we explicitly write down

$$M_{\rm ej} = \int dt \frac{L_{\rm f,iso}}{\Gamma_{\rm f0} c^2},\ \ m_{\rm ext} = \int 4\pi R_{\rm f}^2 m_p n_{\rm ext} dR_{\rm f}, \tag{7}$$

where $L_{\rm f,iso} = L_{\rm f}/(\theta_{\rm f}^2/2)$ is the isotropic jet luminosity given jet opening angle $\theta_{\rm f}$, and $\Gamma_{\rm f0}$ is the jet initial Lorentz factor before deceleration. From the perspective of energy conservation, the change of $\mathcal{E}_{\rm f,iso}$ is

$$d\mathcal{E}_{\rm f,iso} = c^2 dm_{\rm ext} + L_{\rm f,iso} dt. \tag{8}$$

In this expression, the first term accounts for the energy by accumulating external mass into the jet whereas the second component demonstrates the persistent energy injection from the central engine.

Combining Equations (6), (7), and (8), we obtain a differential equation for the jet deceleration,

$$\frac{d\Gamma_{\rm f}}{dm_{\rm ext}} = -\frac{4\Gamma_{\rm f}^5 - (5 + 3A_{\rm inj})\Gamma_{\rm f}^3 + \Gamma_{\rm f}}{3M_{\rm ej}\Gamma_{\rm f}^3 - 2m_{\rm ext} + 8\Gamma_{\rm f}^4 m_{\rm ext}}, \tag{9}$$

which resembles the formulation for GRBs (e.g., Zhang et al. 2021), with the exception of an additional correction factor arising from continuous energy and mass injection,

$$A_{\rm inj} = \left(1 - \frac{\Gamma_{\rm f}}{\Gamma_{\rm f0}}\right)\frac{L_{\rm f,iso}}{c^2}\left(\frac{dm_{\rm ext}}{dt}\right)^{-1}. \tag{10}$$

To numerically solve Equation (9), we connect the jet radius to the SMBH rest-frame time t, e.g.,

$$dR_{\rm f} = \frac{\beta_{\rm f} c dt}{1 - \beta_{\rm f}}, \tag{11}$$

where $\beta_{\rm f} = \sqrt{1 - \Gamma_{\rm f}^{-2}}$.

To test the impact of time-dependent power injection rates, we show in Figure 2 the time evolution of the jet Lorentz factor using a simple density profile with $k = 0$ and $n_{\rm ISM} = 2\ {\rm cm}^{-3}$ for the fast jet case. We fix the initial jet Lorentz factor to be $\Gamma_{\rm f0} = 30$ and use the values $\eta_{\rm f} = 0.12$ and $\theta_{\rm f} = 0.15$ obtained from the X-ray data fitting in Section 4. From the thin red curve to the thick black curve, the parameter α varies from 0 to 0.8. The vertical orange dashed line depicts the fallback time whereas the yellow area represents the time window of the X-ray and radio data to be fitted. Initially, the external mass $m_{\rm ext}$ is not high enough to decelerate the jet and the Lorentz factor remains at a constant level, known as the "coasting phase." Deceleration occurs at $t_{\rm dec}$ when $M_{\rm ej}/\Gamma_{\rm f0} \simeq m_{\rm ext}$ is satisfied. The decaying slope of $\Gamma_{\rm f}$ before $t_{\rm fb}$ for each curve in Figure 2 aligns well with the theoretical estimation $\Gamma_{\rm f} \propto t^{-(2+\alpha)/8}$ derived from $\int L_{\rm f,iso} dt \sim 4\pi R_{\rm f}^3 \Gamma_{\rm f}^2 m_p c^2/3$. In this regime, we find the correction factor to be $A_{\rm inj} \lesssim 0.1$. The increasing $M_{\rm ej}$ primarily leads to modifications from continuous injection.

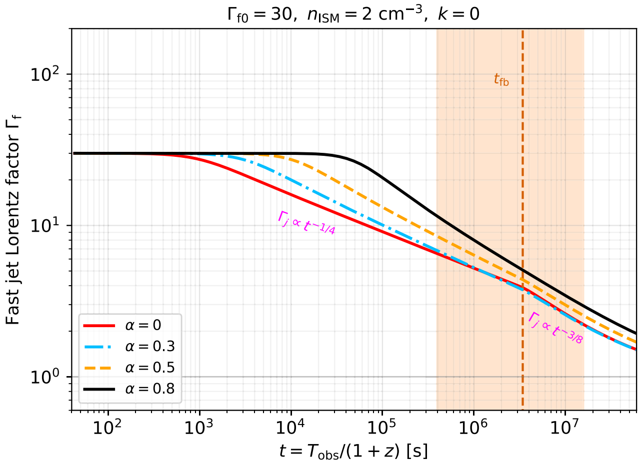

Figure 2. Test time evolution of the fast jet Lorentz factor with persistent power and mass injections for the simple case $k = 0$. From the thin red curve to the thick black curve, α varies from 0 to 0.8. The vertical orange dashed line shows the fallback time, whereas the orange area represents the time window (10 days $\lesssim T_{\rm obs} \lesssim$ 400 days) for the X-ray and radio data fitting.

For $t > t_{\rm fb}$, the energy injection rate decays much faster and the $\Gamma_{\rm f}$ enters the Blandford–McKee (BM) self-similar regime (Blandford & McKee 1976), e.g., the $\Gamma_{\rm f} \propto R_{\rm f}^{-2/3} \propto t^{-3/8}$ predicted by a fixed $\mathcal{E}_{\rm f,iso} \sim 4\pi R_{\rm f}^3 \Gamma_{\rm f}^2 n_{\rm ext} m_p c^2/3$. In this picture, we typically expect two break points at $t_{\rm dec}$ and $t_{\rm fb}$, similar to the red curve in Figure 2. However, for larger α, $t_{\rm dec}$ becomes closer to $t_{\rm fb}$ and the decaying slope $(2+\alpha)/8$ approaches 3/8, which as a result makes the second break at $t_{\rm fb}$ less prominent. We also observe that $\Gamma_{\rm f}(t)$ is very sensitive to α as it approaches 1.

The derivation presented above is also applicable to slow jets by substituting the corresponding physical quantities with those for slow jets., e.g., $\Gamma_{\rm s}$, $L_{\rm s}$, and $\theta_{\rm s}$. For a slow jet with $\Gamma_{\rm s0} = 4$, we estimate the deceleration time $t_{\rm dec,s} \sim 17$ days using

$$\int L_{\rm s,iso} dt = \frac{4\pi}{3-k}\Gamma_{\rm s0}^2 m_p n_{\rm ext}(R_{\rm s}) R_{\rm s}^3 c^2, \tag{12}$$

and the radius $R_{\rm s} \approx 2\Gamma_{\rm s0}^2 ct$. We can also estimate the slow jet radius at $T_{\rm obs} = 100$ days to be $R_{\rm s} \lesssim R_{\rm cnm}$, which implies that the slow jet is propagating within the circumnuclear medium characterized by index $k = 1.8$.

We examined the time evolution of the slow jet and found that it becomes mildly relativistic, e.g., $\Gamma_{\rm s} \simeq 1.4$, by the end of the data-fitting time window. This occurs because the circumnuclear medium density profile $n_{\rm ext} \propto R^{-1.8}$ results in a slowly decelerating jet. In this case, our treatments for relativistic jets still apply to the slow jet.

Table 1
Physical (Fiducial and Fitting) Parameters for the Structured Jet Model

Category	Parameter	Value
Fiducial	$M_{\rm BH}$	$10^7\ M_\odot$
	$M_\star$	$5\ M_\odot$
	$\eta_{\rm acc}$	0.1
	$R_{\rm cnm}$	10^{18} cm
	k	1.8
Fitting Parameters		
Universal	α	0.8
	$n_{\rm ISM}$	2.0 $\rm cm^{-3}$
	s	2.3
Fast, Slow Jets	$\eta_{\rm f,s}$	0.12, 0.04
	$\theta_{\rm f,s}$	0.15, 0.3
	$\Gamma_{\rm f0,\ s0}$	30, 4.0
FS, RS	$\epsilon_e^{\rm fs,\ rs}$	0.1, 0.2
	$\epsilon_B^{\rm fs,\ rs}$	3.0×10^{-3}, 0.1
	$f_e^{\rm fs,rs}$	1.0, 1.5×10^{-3}

So far, we have derived the differential equations for TDE jet evolution, taking in to account the continuous injection rate defined in Equation (1) and Equation (4). In Section 4, we will apply this model to both fast and slow jets with different initial conditions and jet parameters. Subsequently, we will compute the synchrotron and inverse Compton emissions in their respective FS and RS regions.

4. Multizone and Multiwavelength Modeling

In this section, we model the emissions from the FSs and RSs for both fast and slow jets. We apply the structured jet model to fit the X-ray (0.3–10 keV) and radio and millimeter (15.5 GHz and 225 GHz, respectively) lightcurves and spectra. The jets considered in this work are all on axis. We use two sets of jet parameters ($\eta_{\rm f}$, $\theta_{\rm f}$, and $\Gamma_{\rm f0}$) and ($\eta_{\rm s}$, $\theta_{\rm s}$, and $\Gamma_{\rm s0}$) to describe the time evolutions of the fast and slow jets, respectively, as summarized in Table 1.

Regarding the thermal optical emissions, which may stem from the thermalization of emission from an accretion disk or a hot corona, we consider them as upper limits within the multizone model.

4.1. Jet Forward Shock and Reverse Shock Modeling

For simplicity, we continue using the fast jet as an example, noting that the FS and RS models presented here are also applicable to slow jets by substituting the corresponding physical quantities with those for slow jets.

We also note that we use the single-zone approximation for each shock component, in the sense that we do not consider integration over the equivalent arrival time surface. Our model is regarded as a multizone model in light of FS and RS regions of fast and slow jets.

FS. In the jet FS model, given the external particle number density $n_{\rm ext}$ and $\Gamma_{\rm f}$, we parameterize the magnetic field strength of the downstream magnetic field as $B_{\rm f,fs} = [32\pi\Gamma_{\rm f}(\Gamma_{\rm f}-1)\epsilon_B^{\rm fs} n_{\rm ISM} m_p c^2]^{1/2}$, where $\epsilon_B^{\rm fs}$ represents the fraction of internal energy density that goes into the magnetic field energy density. We consider shock-accelerated nonthermal electrons, described by a power-law injection rate, e.g., $\dot{Q}_{e,\rm fs}(\gamma_e) \propto \gamma_e^{-s}$, where γ_e is the electron Lorentz factor and $s \geqslant 2.0$ is the spectral index. To normalize the injection rate, we introduce the number fraction ($f_e^{\rm fs}$) of the downstream electrons that are accelerated and the energy fraction ($\epsilon_e^{\rm fs}$) of the internal energy that is deposited to nonthermal electrons. In this approach, we infer the minimum Lorentz factor for injected electrons

$$\gamma_{e,m}^{\rm fs} = (\Gamma_{\rm f} - 1) g(s) \frac{\epsilon_e^{\rm fs}}{f_e^{\rm fs}} \frac{m_p}{m_e}, \tag{13}$$

where $g(s) = (s-2)/(s-1)$ for $s > 2.0$ and $g(s) \sim \mathcal{O}(0.1)$ for $s = 2.0$. We then normalize $Q_{e,\rm fs}$ via

$$(4\pi R_{\rm f}^2 t'_{\rm f,dyn} c) \int \dot{Q}_{e,\rm fs} d\gamma_e = \frac{4\pi f_e^{\rm fs} R_{\rm f}^3 n_{\rm ext}}{3 t'_{\rm f,dyn}}, \tag{14}$$

where $t'_{\rm f,dyn} = R_{\rm f}/(\Gamma_{\rm f} c)$ is the dynamic time measured in the comoving frame.

RS. For the RS, we parameterize the magnetic field strength and electron injection rate for the RSs, e.g., $B_{\rm f,rs}$ and $\dot{Q}_{e,\rm rs}$. In contrast to the FS scheme, the relative Lorentz factor between the RS up and downstream is $\Gamma_{\rm f,rs-rel} \approx (\Gamma_{\rm f0}/\Gamma_{\rm f} + \Gamma_{\rm f}/\Gamma_{\rm f0})/2$. Similar to the FS case, we define the RS parameters $\epsilon_e^{\rm rs}$, $f_e^{\rm rs}$, and $\epsilon_B^{\rm rs}$. In this case, the magnetic field strength of the RS region can be written as

$$B_{\rm f,rs} = \sqrt{32\pi\epsilon_B^{\rm rs}\Gamma_{\rm f,rs-rel}(\Gamma_{\rm f,rs-rel} - 1) n'_{\rm f0} m_p c^2}, \tag{15}$$

where $n_{\rm f0}' = L_{\rm f,iso}/(4\pi\Gamma_{\rm f0}^2 R_{\rm f}^2 m_p c^3)$ is the comoving upstream number density of the RS. The minimum Lorentz factor of the injected electrons in the RS, e.g., $\gamma_{e,m}^{\rm rs}$ can be obtained by replacing $\Gamma_{\rm f}$ with $\Gamma_{\rm f,rs-rel}$ in Equation (13). Moreover, the particle number injection rate $\dot{N}_{\rm rs} = L_{\rm f,iso}/(\Gamma_{\rm f0} m_p c^2)$ should be used to normalize $\dot{Q}_{e,\rm rs}$, which can be expressed explicitly as

$$(4\pi R_{\rm f}^2 t'_{\rm f,dyn} c) \int \dot{Q}_{e,\rm rs} d\gamma_e = f_e^{\rm rs} \dot{N}_{\rm rs} = \frac{f_e^{\rm rs} L_{\rm f,iso}}{\Gamma_{\rm f0} m_p c^2}. \tag{16}$$

Given the injected electron rates and the magnetic fields in FSs and RSs, we use the AM^3 software (Klinger et al. 2023) to model the synchrotron and synchrotron self-Compton emissions in these two regions by numerically solving the corresponding time-dependent transport equations for electrons in the comoving frame,

$$\frac{\partial n'_e}{\partial t'} = \dot{Q}_e - \frac{\partial}{\partial \gamma_e}(\dot{\gamma}_e n'_e) - \frac{n'_e}{t'_{\rm f,dyn}}. \tag{17}$$

In this equation, n'_e and t' represent the electron number density (differential in Lorentz factor and volume) and time measured in the comoving jet frame, respectively, and $\dot{\gamma}_e \sim \gamma_e({t_{e,\rm sy}}'^{-1} + {t_{e,\rm ic}}'^{-1})$ is the electron energy loss rate due to synchrotron and inverse Compton radiation in the synchrotron self-Compton diagram. In addition, we self-consistently estimate the electron maximum Lorentz factor by balancing the efficient acceleration rate $t_{e,\rm acc}'^{-1} \sim eB_{\rm f}/(\gamma_e m_e c)$ and the cooling rate $t_{e,c}'^{-1} = t_{e,\rm sy}'^{-1} + t_{e,\rm ic}'^{-1}$. To get the observed photon spectra, we convert the obtained comoving photon density spectrum $n'_\gamma = d^2 N_\gamma/(d \ln E'_\gamma dV')$ in units of $\rm cm^{-3}$ to the flux in the observer frame via

$$\nu F_\nu(E_{\gamma,\mathrm{obs}}) = f_{\mathrm{br}}\,\Gamma_{\mathrm{f}}^2\left(\frac{R_{\mathrm{f}}^2}{d_L^2}\right) c E'_\gamma n'_\gamma \exp(-\tau_{\mathrm{EBL}}), \tag{18}$$

where the observed and comoving energies are connected by $E_{\gamma,\mathrm{obs}} = \Gamma_{\mathrm{f}} E'_\gamma/(1+z)$, $f_{\mathrm{br}} = 1/[1 + (\Gamma_{\mathrm{f}}\theta_{\mathrm{f}})^{-2}]$ accounts for the jet break correction, and we also applied the correction of $\gamma\gamma$ absorption attributed to attenuation by extragalactic background light (EBL) during propagating from $z = 1.19$ ($d_L \simeq 8.4$ Gpc) to the Earth.

4.2. Fast Jet: X-Ray Data Fitting

We apply the dynamics of the fast and slow jets (Section 3.2) together with the modeling of the FSs and RSs to explain the measured 0.3–10 keV lightcurve and the X-ray spectra in multiple epochs (Andreoni et al. 2022; Pasham et al. 2023; Yao et al. 2024), e.g., $T_{\mathrm{obs}} = 15-16$ days, 25−27 days, and 41−46 days. To reduce the free parameters, we assume the FSs of the fast and slow jets share the same ϵ_e^{fs}, ϵ_B^{fs}, and f_e^{fs}, whereas all RSs have the same ϵ_e^{rs}, ϵ_B^{rs}, and f_e^{rs}.

We fix the spectral index of injected electrons to be $s = 2.3$ during our calculation. The fiducial parameters for the TDE accretions and the external density profile, together with the physical parameters of the jets and the RSs and FSs obtained by fitting the X-ray, radio, and millimeter spectra and lightcurve, are presented in Table 1.

Figure 3 shows the fitting to the SED in three epochs, $T_{\mathrm{obs}} = 12-15$ days, 25−27 days, and 41−46 days, respectively, in the top, middle, and bottom panels. The X-ray (black points), optical (orange points), and radio and millimeter (blue points) are sourced from Andreoni et al. (2022) and Pasham et al. (2023), whereas the hard X-ray data (gray points; Yao et al. 2024) at the closest observation windows are also shown. In the fast jet (denoted as "F.Jet") scenario, the thin and thick blue dashed curves depict the combined synchrotron and inverse Compton (denoted as "SY/IC") emissions from the FS and RS regions. From this figure, we find that, by adopting the parameters in Table 1, the RS fast-cooling synchrotron spectra are consistent with the observed X-ray data. We also observe that the FS is subdominant using the parameters from the radio data fitting. The FS and RS spectra are also consistent with the analytical predictions in Appendix B.

In Figure 4, we present the fitting to the measured X-ray lightcurve (Yao et al. 2024) using the jet scenario in the lower panel. Our results indicate that emissions from the fast jet RS could account for the fast-decaying X-ray lightcurve, since the decaying accretion rate defined in Equation (1) can directly influence the injection rate of the accelerated electrons. As we observed that the FS is subdominant in the X-ray bands and predicts a more flat lightcurve, its lightcurve is not displayed in this figure.

To comprehend the temporal evolution of these regions, we derive analytical X-ray lightcurves considering the time-dependent energy injection luminosity before and after the fallback time. Requiring $\Gamma_{\mathrm{f}} = 1/\theta_{\mathrm{f}}$, we infer the fast jet break time to be $t_{\mathrm{br}} \simeq 2.8\times10^6$ s for $\theta_{\mathrm{f}} = 0.15$, which is close to the fallback time t_{fb}. For simplicity, in the following discussions, we do not distinguish between t_{fb} and t_{br}, and treat the jet as postbreak and apply the steepening factor $f_{\mathrm{br}} = (\Gamma_{\mathrm{f}}\theta_{\mathrm{f}})^2 \propto T_{\mathrm{obs}}^{-3/4}$ to the lightcurve after t_{fb}. In this case, the analytical X-ray lightcurves for both FSs and RSs in the fast-cooling regime can be written, respectively, as

$$\nu F_\nu^{(\mathrm{fs})} \propto \begin{cases} f_{\mathrm{br}}\, T_{\mathrm{obs}}^{-\alpha+1-s/2}, & T_{\mathrm{obs}} < T_{\mathrm{br}} \simeq T_{\mathrm{fb}}, \\ f_{\mathrm{br}}\, T_{\mathrm{obs}}^{-1}, & T_{\mathrm{obs}} > T_{\mathrm{br}} \simeq T_{\mathrm{fb}}, \end{cases} \tag{19}$$

and

$$\nu F_\nu^{(\mathrm{rs})} \propto \begin{cases} T_{\mathrm{obs}}^{-[5\alpha+\alpha(s-1)]/4}, & T_{\mathrm{obs}} < T_{\mathrm{br}} \simeq T_{\mathrm{fb}}, \\ T_{\mathrm{obs}}^{-(2s+25)/12}, & T_{\mathrm{obs}} > T_{\mathrm{br}} \simeq T_{\mathrm{fb}}, \end{cases} \tag{20}$$

where $T_{\mathrm{br}} = (1+z)t_{\mathrm{br}}$, $T_{\mathrm{fb}} = (1+z)t_{\mathrm{fb}}$, and a detailed derivation is provided in Appendix B. They are consistent with the GRB afterglow lightcurves for both FSs and RSs (see Zhang 2018, for details). Since we adopted the approximations $\Gamma_{\mathrm{f,\ rs-rel}} \sim \Gamma_{\mathrm{f,\ rs-rel}} - 1 \sim \Gamma_{\mathrm{f0}}/(2\Gamma_{\mathrm{f}})$, to obtain Equation (20), the numerical time decay slope could be steeper by a correction factor $\sim T_{\mathrm{obs}}^{-0.2} - T_{\mathrm{obs}}^{-0.4}$. The analytical lightcurves closely match the numerical results obtained using $\alpha = 0.8$ in Figure 4. Specifically, the jet break time in the observer frame, $T_{\mathrm{br}} \simeq 72$ days, and the steepened temporal evolution for $s = 2.3$, such as $\propto T_{\mathrm{obs}}^{-2.7} - T_{\mathrm{obs}}^{-2.9}$, after T_{br}, are consistent with the X-ray fluxes in the time window $T_{\mathrm{br}} < T_{\mathrm{obs}} < 200$ days and the late-time upper limits (illustrated as red triangles; Eftekhari et al. 2024) extending to $T_{\mathrm{obs}} \sim 400$ days. Conversely, the FS is disfavored due to its relatively flat temporal evolution and negligible flux in the X-ray bands.

We emphasize that there is no necessary physical causation for the relation $T_{\mathrm{br}} \simeq T_{\mathrm{fb}}$. The mass fallback time is determined by the SMBH mass and the structure of the disrupted star, such as $M_\star$ and $R_\star$. Since we use fiducial parameters for these quantities, the mass fallback time is roughly fixed and does not depend on our fitting parameters. As for the jet break time, we found that $T_{\mathrm{br}} \sim T_{\mathrm{fb}}$ is favored for fitting the X-ray lightcurve. For example, a later T_{br} would exceed the late-time X-ray upper limits, whereas an earlier T_{br} would underestimate the X-ray flux at $T_{\mathrm{obs}} \sim 100$ days.

4.3. Slow Jet: Radio and Millimeter Data Fitting

Recently, Matsumoto & Metzger (2023), Yao et al. (2024), and Zhou et al. (2024) demonstrated that jet FSs, similar to those in GRB afterglow models, can interpret the radio observations of AT 2022cmc. The radio spectra and lightcurves are well described by a decelerated, mildly relativistic jet with an initial Lorentz factor of ∼3−10 in a circumnuclear medium characterized by an index of $1.5 \lesssim k \lesssim 2$. In this work, we aim to provide a more comprehensive model of the multiwavelength emissions from jetted TDEs by considering a slow jet (in addition to the fast jet used for the X-ray data fitting) propagating within R_{cnm}. This approach is consistent with previous studies. The major difference in our work is the inclusion of persistent energy injection due to long-lasting accretion activities, as discussed in Section 3.2.

Similar to the fast jet scenarios, we self-consistently compute the time-dependent synchrotron and inverse Compton emissions in the FS and RS regions, as discussed in Section 4.1. By fitting the radio observations, we obtain the slow jet parameters (η_{s}, θ_{s}, and Γ_{s0}) and the FS parameters (ϵ_e^{fs}, ϵ_B^{fs}, and f_e^{fs}), as summarized in Table 1. Comparing to the fast $\Gamma_{\mathrm{f0}} = 30$ and narrow ($\theta_{\mathrm{s}} = 0.15$) jet considered in Section 4.3, a slow

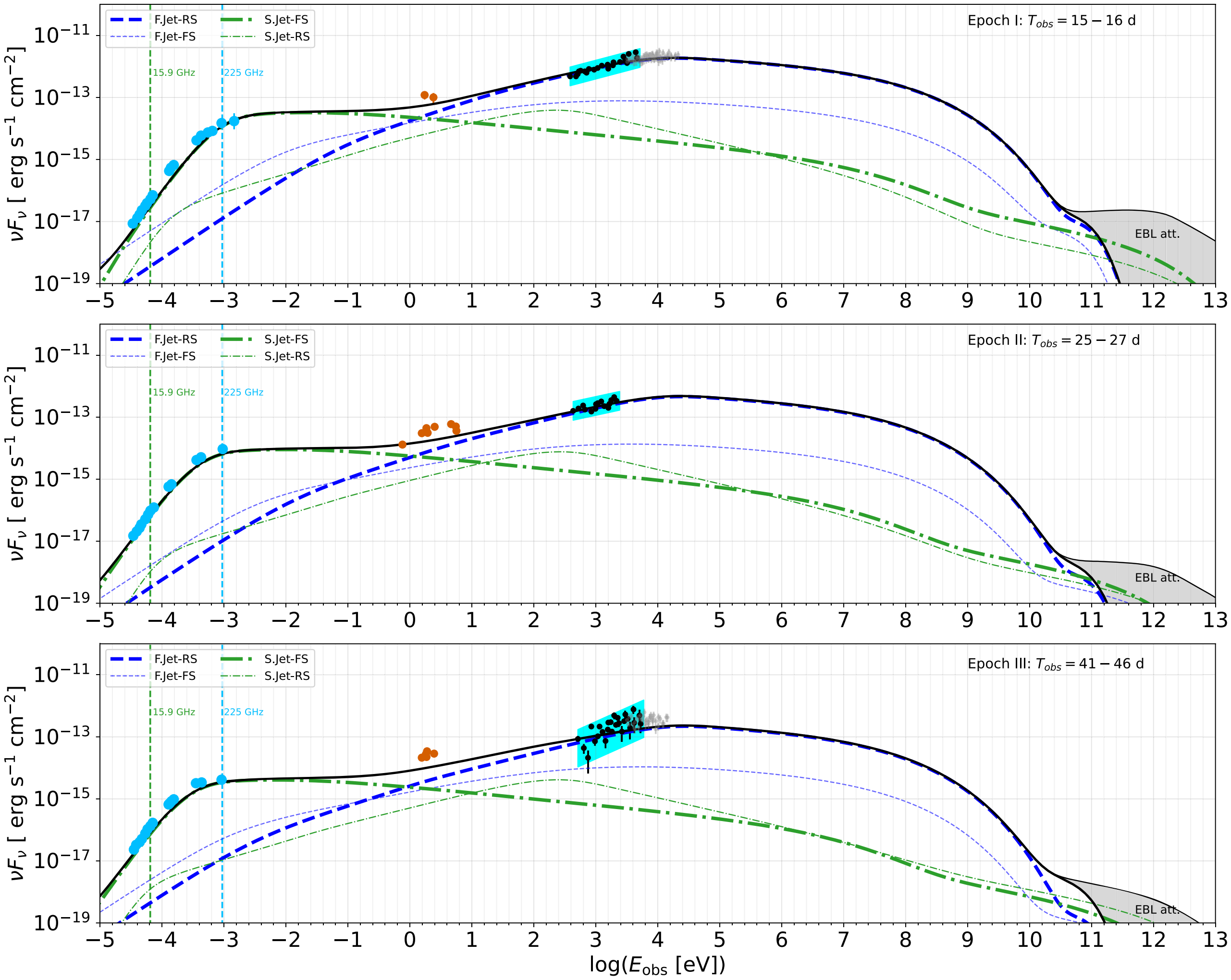

Figure 3. Spectral fitting for three epochs. The "SY/IC" spectra of the fast/slow jet FSs (F.Jet/S.Jet-FS) and RSs (F.Jet/S.Jet-RS) are illustrated. The orange points depict the energy fluxes in optical bands, which are considered as upper limits. The thin and thick solid black curves correspond to the overall SED before and after applying $\gamma\gamma$ attenuation by EBL. The radio and millimeter and X-ray data are depicted as blue and black dots, respectively (Andreoni et al. 2022; Pasham et al. 2023). Additionally, the hard X-ray energy fluxes (Yao et al. 2024) are also shown as gray points.

($\Gamma_{s0} = 4$) and wide ($\theta_s = 0.3$) jet is favored to fit the radio data. For completeness, we incorporate the RS parameters obtained from X-ray data fitting in the fast jet scenario to account for the contribution from the slow jet RS regions.

The fitted FS synchrotron and inverse Compton spectra in the slow jet scenario are shown as the thick green dashed–dotted curves in Figure 3 together with the observed radio to millimeter SED (blue points) and the RS components (thin green dashed–dotted curves). In Figure 4, we also compare our model-predicted 15.5 GHz (green curve) and 225 GHz (blue curve) lightcurves with the corresponding observations. Our results demonstrate that the FS of the continuously powered slow jet can reproduce the observed radio-to-millimeter spectra and lightcurves. Our results and parameters are consistent with Matsumoto & Metzger (2023), and the cumulative slow jet energy,

$$\mathcal{E}_{\rm s,iso} = \frac{2\eta_{\rm s}\dot{M}_{\rm BH}(t_{\rm fb})c^2 t_{\rm fb}}{(1-\alpha)\theta_{\rm s}^2} \sim 8 \times 10^{53}\ {\rm erg}. \tag{21}$$

To understand the radio spectra fitting, we estimate the synchrotron characteristic frequency and the cooling frequency in the FS region to be, respectively,

$$\nu_m = \frac{3\Gamma_{\rm s}(\gamma_{e,{\rm m}}^{\rm fs})^2 eB_{\rm s,fs}}{4\pi(1+z)m_e c} \simeq 3.8 \times 10^2\ {\rm GHz} \times \left(\frac{T_{\rm obs}}{15\ {\rm days}}\right)^{-0.9}\left(\frac{\Gamma_{\rm s}}{3}\right)^{2.2}, \tag{22}$$

and

$$\nu_c = \frac{3\Gamma_{\rm s}\gamma_{e,c}^2 eB_{\rm s,fs}}{4\pi(1+z)m_e c} \simeq 3.1 \times 10^4\ {\rm GHz} \times \left(\frac{T_{\rm obs}}{15\ {\rm days}}\right)^{0.7}\left(\frac{\Gamma_{\rm s}}{3}\right)^{1.4}, \tag{23}$$

where $\gamma_{e,c} \sim 6\pi m_e c/(\sigma_T B_{\rm s,fs}^2 \Gamma_{\rm s} t)$ is the electron cooling Lorentz factor and σ_T is the Thomson cross section. The wind synchrotron and inverse Compton spectra in Figure 3 are consistent with the weak SSA in the electron slow-cooling regime, e.g., the absorption frequency $\nu_a < \nu_m < \nu_c$, characterized by a steep increasing tail, e.g., $\nu F_\nu \propto \nu^3$ for $\nu < \nu_a$. Another mechanism that may prevent the radio emission from escaping is free–free

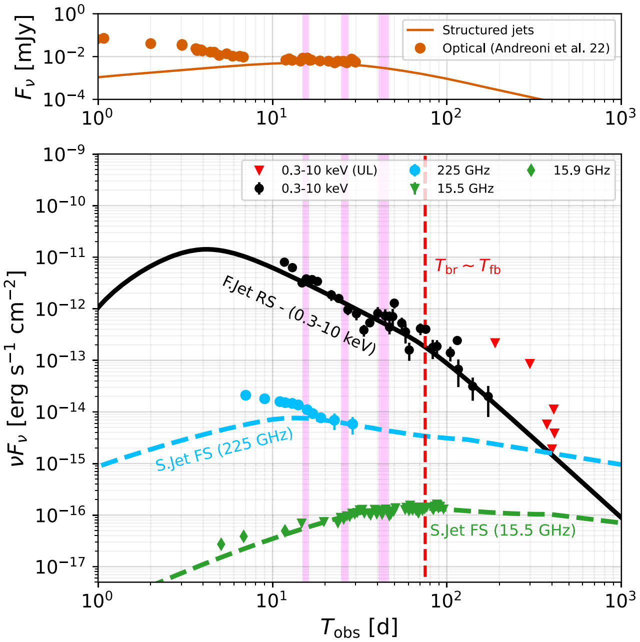

Figure 4. Top panel: comparison of the model-predicted optical lightcurve (orange solid curve) to the observations (orange points). Bottom panel: fitting of nonthermal X-ray and radio lightcurves using the parameters in Table 1. The solid black line represents the 0.3–10 keV X-ray afterglow from the fast jet's RS model (F.Jet RS). The blue and green dashed curves depict the 225 GHz and 15.9 GHz lightcurves obtained from the slow jet FS (S.Jet FS) scenario. The vertical magenta areas represent the three epochs of SED fitting in Figure 3. The latest X-ray upper limits (ULs) are depicted as red triangles. The vertical red line represents the fast jet break time ($T_{\rm br}$), which is close to the fallback time ($T_{\rm fb}$). Data sources: Andreoni et al. (2022), Pasham et al. (2023), Eftekhari et al. (2024), and Yao et al. (2024)

absorption due to thermal electrons in the external medium, which typically requires very high $n_{\rm ext}$. Applying Equation (3), we find that the free–free optical depth, $\tau_{\rm ff} \propto n_{\rm ext}^2$ (e.g., Murase et al. 2017), is extremely low, and conclude that this effect is negligible in the radio data fitting.

The slow jet FS model can explain the 225 GHz and 15.5 GHz fluxes and lightcurves very well after $T_{\rm obs} = 15$ days. However, the early-stage radio and millimeter fluxes for $T_{\rm obs} < 15$ days are underestimated by the slow jet FS model, as illustrated in Figure 4. This suggests that the early-time radio emissions may originate from different zones, such as a structured two-component outflow (Sato et al. 2024; Zhou et al. 2024). Regarding the slow jet RS component, the use of a very small $f_e^{\rm rs}$ results in a very high minimum Lorentz factor for the accelerated electrons. Consequently, the corresponding synchrotron and inverse Compton spectra peak at much higher energies compared to the FS case, e.g., the thin green dashed–dotted curves in Figure 3, and the RS contribution to the radio and millimeter energy fluxes is minimal.

Overall SEDs. We have presented a comprehensive discussion of the FS and RS components in the fast and slow jets. Combining the emissions from these zones, we obtain the overall SED for the three epochs before and after applying EBL absorption. These are respectively represented by the thin and thick black solid curves in Figure 3. For reference, the thermal optical data (orange points) are also included as upper limits, since the UV and optical light may come from different zones, such as a thermal envelope with radius $\sim 10^{15}$ cm (Yao et al. 2024). The contribution of the jets to the optical bands is consistent with optical observations (see also the upper panel of Figure 4), which further supports fast-cooling synchrotron emission being the origin of the X-rays. Importantly, our multizone model, incorporating the FSs and RSs of both fast and slow jets, effectively describes the multiwavelength observations, encompassing radio and X-ray spectra, along with their corresponding lightcurves.

5. Discussion

We have analyzed both FS and RS scenarios for both fast and slow jets, identifying the RS of the fast jet and the FS of the slow jet regions as promising X-ray and radio sources for the jetted TDE AT 2022cmc. Their primary advantages are summarized below.

1. *Fast jet RS.* The combination of continuously decaying energy injection and deceleration in the ISM leads to a rapidly decaying X-ray lightcurve, consistent with observations. Fitting the spectra requires a low value of $f_e^{\rm rs} = 1.5 \times 10^{-3}$, which predicts a high $\gamma_{e,m}^{\rm rs}$. This value is consistent with values suggested from the RS model for early GRB afterglow emission (Genet et al. 2007) and could be related to the injection physics of the RS of magnetically dominated jets.
2. *Slow jet FS.* The typical values of $\epsilon_B^{\rm fs} = 3.0 \times 10^{-3}$ and $f_e^{\rm fs} = 1$, consistent with GRB afterglow modeling, along with the presence of a dense external medium, facilitate the consistency of SSA with the radio spectra. Additionally, the radio and millimeter lightcurves can be effectively modeled by deceleration of a jet within a circumnuclear medium ($R_{\rm s} \lesssim R_{\rm cnm}$).

5.1. Fitting Parameters

Mass of the disrupted star. To construct the accretion history of AT 2022cmc, we have initially assumed a disrupted star of 5 $M_\odot$ in Equation (1). A lower limit for $M_\star$ can be estimated based on the isotropic-equivalent X-ray luminosity, e.g., $L_{X,\rm iso} \sim 3 \times 10^{47} {\rm erg\ s^{-1}} (T_{\rm obs}/5\ {\rm days})^{-2}$ (Andreoni et al. 2022), which implies an X-ray energy $E_{X,\rm iso} \gtrsim 1.3 \times 10^{53}$ erg. Using the energy conversion efficiencies, the mass of the disrupted star can be estimated as

$$M_\star \sim \frac{2 f_{\rm bol} f_b E_{X,\rm iso}}{\eta_{\rm acc} \eta_{\rm f} \epsilon_e^{\rm fs} c^2} \gtrsim 3.3 M_\odot \eta_{\rm acc,-1}^{-1} \eta_{\rm f,-1}^{-1}, \tag{24}$$

where $f_{\rm bol} \sim 3$–4 is a bolometric correction factor and $f_b = \theta_{\rm f}^2/2$ is the jet beaming factor. Additionally, when lower accretion and jet efficiencies are used, a significantly more massive star is needed to explain the bright X-ray emissions. As a result, the likelihood of such disruptions would decrease notably. Thus, our fiducial values for $M_\star$, $\eta_{\rm acc}$, and $\eta_{\rm f}$ are reasonable rather than optimistic.

Number of parameters. In addition to the fiducial parameters fixed or constrained by observations, e.g., $M_{\rm BH}$ and $M_\star$, and by theoretical estimations, e.g., $R_{\rm cnm}$, k, and $\eta_{\rm acc}$, there are three global parameters: $n_{\rm ISM}$, α, and the spectral index s. For the X-ray data fitting with the fast jet, the free parameters are the jet evolution parameters ($\Gamma_{\rm f0}$, $\eta_{\rm f}$, and $\theta_{\rm f}$) and RS parameters ($\epsilon_e^{\rm rs}$, $\epsilon_B^{\rm rs}$, and $f_e^{\rm rs}$). Similarly, for the slow jet and radio data fitting, there are six parameters: ($\Gamma_{\rm s0}$, $\eta_{\rm s}$, and $\theta_{\rm s}$) and FS parameters ($\epsilon_e^{\rm fs}$, $\epsilon_B^{\rm fs}$, and $f_e^{\rm fs}$). Our degrees of freedom for the radio data fitting are consistent with previous works where $n_{\rm cnm}$, k, $E_{\rm iso}$, θ_j, s, Γ, ϵ_e, ϵ_B, and $\gamma_{e,\rm min}$ are typically needed to explain radio observations (e.g., Matsumoto & Metzger 2023). The jet isotropic-equivalent energy $E_{\rm iso}$ encodes $\eta_{\rm s}$ and $\theta_{\rm s}$, which determine the energy deposited into the jet. Meanwhile, we have used f_e to parameterize the electron minimum energy $\gamma_{e,\min}$. Therefore, we have not introduced extra degrees of freedom to fit the observations in one specific band.

Parameter degeneracy. The fitting parameters summarized in Table 1 are obtained through theoretical estimations and manual adjustments. As discussed in the text, these parameters play a key role in determining the spectra and lightcurve shapes and flux levels. For instance, $\theta_{\rm f}$ influences both $L_{\rm f,iso}$ and the jet break time through the beaming factor $\theta_{\rm f}^2/2$ and the jet break condition $\theta_{\rm f}\Gamma_{\rm f}=1$. The initial Lorentz factor $\Gamma_{\rm f0}$ determines the jet deceleration time and, consequently, the peak of the X-ray lightcurve. Additionally, α affects the slope of the X-ray lightcurve for $T_{\rm obs}\lesssim T_{\rm fb}$. Within the data-fitting time window, $\Gamma_{\rm f}$ converges to the behavior in the deceleration phase and does not depend strongly on $\Gamma_{\rm f0}$. Therefore, we can roughly determine the values for (α, $\eta_{\rm f}$, $\Gamma_{\rm f0}$, and $\theta_{\rm f}$) from the X-ray lightcurve fitting. The remaining parameters (s, $\epsilon_e^{\rm rs}$, $\epsilon_B^{\rm rs}$, and $f_e^{\rm rs}$) primarily control the spectral shape. Specifically, $\gamma_{e,\rm m}^{\rm rs}$ is sensitive to $f_e^{\rm rs}$ rather than $\Gamma_{\rm f,\ rs-rel}$, and s, which, together with $\epsilon_B^{\rm rs}$, determine the synchrotron peak via $\nu_{\rm m}\propto(\gamma_{e,\rm m}^{\rm rs})^2 B_{\rm f,rs}$. Based on current observations, it is challenging to determine $f_e^{\rm rs}$ due to its degeneracy with $\epsilon_B^{\rm rs}$ and $\epsilon_e^{\rm rs}$, as studied in the context of GRBs (Eichler & Waxman 2005). Nevertheless, a smaller $f_e^{\rm rs}<0.01$ is preferred to fit the X-ray spectra. Overall, the joint spectral and lightcurve fitting can reduce the degeneracy of the entire parameter space to some extent. We expect the degeneracy of the slow jet parameters to be comparable with those of the fast jet and previous work where analogous FS models are adopted (e.g., Matsumoto & Metzger 2023; Zhou et al. 2024) .

5.2. Multiwavelength Signatures

X-ray variability. In addition to its rapid decay, another significant feature of the observed X-ray lightcurve is its rapid variability, characterized by a timescale of $\Delta T_{\rm var}\sim 10^3$ s (Yao et al. 2024). However, since we have assumed a homogeneous RS downstream without considering small-scale plasma fluctuations, the intrinsic variability timescale of the RS is much longer than $\Delta T_{\rm var}$

$$\Delta T_{\rm var,rs}=(1+z)\frac{R_{\rm f}}{\Gamma_{\rm f}^2\beta_{\rm f}c}\sim T_{\rm obs}\gg 10^3\ {\rm s}. \quad (25)$$

This indicates that the fast variability cannot be attributed solely to the fast jet RS region. In the RS scenario, since the central engine is active, afterglow variabilities might arise when a late-time outflow from the central engine collides with a preceding blast wave, resulting in a variability timescale down to the light-crossing time of the central engine (Ioka et al. 2005). Furthermore, the physical characteristics of the RS region depend sensitively on $L_{\rm f,iso}$, which can be modulated by accretion at the horizon of the SMBH (Reis et al. 2012), leading to rapid variations on the timescale $\Delta T_{\rm var,eng}\sim(1+z)R_{\rm Sch}/c\sim 10^3$ s, where $R_{\rm Sch}$ is the Schwarzschild radius. Overall, the continuously powered RS scenario predicts both long-term (e.g., $\Delta T_{\rm var,rs}$) and rapid (e.g., $\Delta T_{\rm var,eng}$) X-ray variabilities, stemming from the RS downstream and the central engine, respectively.

Late-time X-ray upper limits. Recently, Eftekhari et al. (2024) reported late-time X-ray upper limits in the 0.3–10 keV band extending to $T_{\rm obs}\sim 400$ days. These upper limits reveal a further steepened X-ray lightcurve, which was interpreted as the cessation of jet activity at $T_{\rm obs}\sim 215$ days, when the accretion rate becomes sub-Eddington. In this paper, we have demonstrated that the steepening can also be alternatively explained by a jet break occurring at an earlier time, e.g., $T_{\rm br}\simeq 72$ days. The late-time upper limits and the data points in the time interval $T_{\rm br}\lesssim T_{\rm obs}\lesssim 400$ days can be well described by the steepened lightcurve in the jet RS scenario (see Figure 4).

Radio and millimeter emissions. We have shown that the radio spectra and lightcurves can be effectively described by the slow jet FS regions. However, the model-predicted early time radio and millimeter energy fluxes fall below the measurements. This issue has also been noted in Sato et al. (2024) and Zhou et al. (2024), where additional components or radiation zones are introduced to account for the early time radio emissions. This suggests that the radio signals of TDEs may have a more complex origin.

γ-ray detectability. Using the same parameters for the jet FS, we have obtained the energy flux $\nu F_\nu\sim 10^{-14}-10^{-13}$ erg s^{-1} cm^{-2} in the Fermi Large Area Telescope (Fermi-LAT) γ-ray band (0.1$-$10 GeV). The nondetection of γ-ray sources by Fermi within a 1° diameter of AT 2022cmc sets an upper limit on the energy flux $\nu F_\nu<8.8\times10^{-9}$ erg s^{-1} cm^{-2} (Pasham et al. 2023), which is much higher than the γ-ray energy flux predicted by our wind–jet model. Since the FS lightcurve maintains a shallow decay before $T_{\rm br}$, we roughly estimate the 100 day detection horizon for AT 2022cmc-like TDEs for Fermi-LAT in the optimistic case of $z\lesssim 0.17$. This corresponds to an occurrence rate of approximately $\lesssim$0.02$-$0.1 yr^{-1}, using a rate density of $0.02^{+0.04}_{-0.01}$ Gpc^{-3} yr^{-1} (Andreoni et al. 2022). We infer that it is difficult for Fermi-LAT to detect jetted TDE as luminous as AT 2022cmc within one decade, unless a much more efficient energy conversion in the FS region is attained.

Multimessenger implications. Since the identification of the first TDE with an IceCube neutrino association, AT 2019dsg (Stein et al. 2021), more neutrino-coincident TDE candidates have been identified, such as AT 2019fdr (Reusch et al. 2022), AT 2019aalc (van Velzen et al. 2024), two dust-obscured ones (Jiang et al. 2023), and AT 2021lwx (Yuan et al. 2024). Relativistic jets (Wang & Liu 2016; Dai & Fang 2017; Lunardini & Winter 2017; Senno et al. 2017), subrelativistic winds (Liu et al. 2020; Murase et al. 2020; Winter & Lunardini 2021, 2023; Yuan & Winter 2023), and accretion flows (Murase et al. 2020; Hayasaki 2021) have been studied as the origin of TDE neutrinos. For AT 2022cmc, we have tested the neutrino fluences using an efficient cosmic-ray injection in the jet–wind model, where most of the jet power is converted to nonthermal protons. Our results demonstrate a very low neutrino fluence due to the relatively high redshift and less dense target photons, compared to AT 2019dsg, AT 2019fdr, and AT 2019aalc (e.g., Murase et al. 2020; Winter & Lunardini 2023; Yuan & Winter 2023).

6. Summary and Conclusions

The distinct signatures of the radio, millimeter, optical, UV, and X-ray signals of AT 2022cmc indicate a multicomponent origin. In this work, we have presented a time-dependent structured jet model involving a fast relativistic jet (initial Lorentz factor of 30) and a slow relativistic wind (initial Lorentz factor of 4) to explain the multiwavelength spectral and temporal observations of AT 2022cmc. We have modeled the jet evolution within a generic external medium characterized by a power-law density profile, $n_{\rm ext} \propto R^{-k}$, extending to the ISM. Considering an active central engine powered by continuous accretion characterized by a power-law decaying accretion rate, we have incorporated persistent mass and power injections into the jets, which could significantly affect the dynamics and subsequently the multiwavelength lightcurves before the mass fallback time. For instance, continuous energy and mass injections extend the duration of the RS emissions, enabling explanation of the late-time X-ray observations in the fast jet scenario.

We have self-consistently computed the synchrotron and inverse Compton emissions from the shock-accelerated energetic electrons in the FS and RS regions of the fast and slow jets. We have demonstrated that the X-ray spectra and fast-decaying lightcurves can be well described by the fast jet RS region, whereas the slow jet FS could explain the radio and millimeter observations after $T_{\rm obs} \sim 10$ days. Using the same FS parameters and RSs, our calculation demonstrates that the fast jet FS and the slow jet RS contributions can be subdominant. Specifically, we have observed that the jet FS would result in a more shallowly decaying lightcurve. Notably, the fast jet RS X-ray lightcurve steepening due to the jet break at $T_{\rm br} \simeq 72$ days aligns well with the late-time X-ray energy fluxes and upper limits extending to $T_{\rm obs} \sim 400$ days. Using the same parameters for the jet FS region, we have estimated the γ-ray energy flux in the energy range 100 MeV–10 GeV to be $\sim 10^{-14}$–10^{-13} erg s^{-1} cm^{-2} before $T_{\rm fb}$, which corresponds a detection rate of $\lesssim 0.02$–0.1 per year for AT 2022cmc-like jetted TDEs and is consistent with the nondetection of jetted TDEs by Fermi-LAT. Klein–Nishina suppression to inverse Compton emission together with EBL absorption make it increasingly challenging to detect jetted TDEs in the very high-energy TeV γ-ray range.

Our comprehensive modeling of the structured jet, involving an FS and RS, related to TDEs provides a useful physical framework for interpreting the time-dependent multiwavelength observations of jetted TDEs detected in the future. Meanwhile, this work also provides a prototype to investigate the physical conditions of mass accretion, the ambient gas density profile, and the outflows through spectral and lightcurve fitting.

Acknowledgments

We thank Mahmoud Al-Alawashra for a thorough review of the paper. The work of K.M. is supported by NSF grant Nos. AST-2108466, AST-2108467, and AST-2308021. B.T.Z. and K.M. are supported by KAKENHI grant Nos. 20H01901 and 20H05852.

Appendix A

Evolution of Relativistic Jets with Continuous Energy Injection: The Full Treatment with Forward and Reverse Shocks

We analyze the evolution of a persistently powered fast jet within an external medium $n_{\rm ext}$, accounting for the effects of both FSs and RSs. Figure 5 schematically depicts the physical conditions of this jet, including mass injections, contact discontinuity between the downstreams of RS and FS, and the physical quantities (see the text below for definitions) in different regions. Following the approach used in GRB afterglow modeling (Huang et al. 1999; Pe'er 2012; Nava et al. 2013; Zhang 2018; Zhang et al. 2023), we derive the total energy of the fast jet in the SMBH rest frame,

$$\begin{aligned} \mathcal{E}_{\rm f,iso} = &\ \Gamma_{\rm f0} M_{\rm f} c^2 + \Gamma_{\rm f} M_{\rm rs,d} c^2 + \Gamma_{\rm rs,eff} \mathcal{E}_{\rm rs,in} \\ &+ \Gamma_{\rm f} m_{\rm ext} c^2 + \Gamma_{\rm fs,eff} \mathcal{E}_{\rm ext,in}, \end{aligned} \tag{A1}$$

where $M_{\rm f}$, $M_{\rm rs,d}$, and $m_{\rm ext}$ are the masses of unshocked ejecta, RS downstream, and the FS downstream originating from an external medium, respectively. The downstream internal energies for FS and RS can be written as

$$\begin{aligned} \mathcal{E}_{\rm ext,in} &= (\Gamma_{\rm f} - 1) m_{\rm ext} c^2, \\ \mathcal{E}_{\rm rs,in} &= (\Gamma_{\rm f,rs-rel} - 1) M_{\rm rs,d} c^2, \end{aligned} \tag{A2}$$

where $\Gamma_{\rm f,\ rs-rel} \approx (\Gamma_{\rm f}/\Gamma_{\rm f0} + \Gamma_{\rm f0}/\Gamma_{\rm f})/2$ is the relative Lorentz factor of the RS and adiabatic and radiative energy losses are neglected (see Zhang 2018; Zhang et al. 2023, for details). The effective Lorentz factors are

$$\begin{aligned} \Gamma_{\rm fs,eff} &= (\hat{\gamma}_{\rm fs} \Gamma_{\rm f}^2 - \hat{\gamma}_{\rm fs} + 1)/\Gamma_{\rm f}, \\ \Gamma_{\rm rs,eff} &= (\hat{\gamma}_{\rm rs} \Gamma_{\rm f}^2 - \hat{\gamma}_{\rm rs} + 1)/\Gamma_{\rm f}, \end{aligned} \tag{A3}$$

where the adiabatic indices are defined as $\hat{\gamma}_{\rm fs} = (4\Gamma_{\rm f} + 1)/(3\Gamma_{\rm f})$ and $\hat{\gamma}_{\rm rs} = (4\Gamma_{\rm f,rs-rel} + 1)/(3\Gamma_{\rm f,rs-rel})$.

Considering the energy injection from the SMBH and the swept-up external material, we have the derivative of $\mathcal{E}_{\rm f,iso}$

$$d\mathcal{E}_{\rm f,iso} = c^2 dm_{\rm ext} + L_{\rm f,iso} dt. \tag{A4}$$

We obtain the differential equations for $\Gamma_{\rm f}$ by combining the equations above,

$$\frac{d\Gamma_{\rm f}}{dR_{\rm f}} = -\frac{\overbrace{(\Gamma_{\rm fs,eff} + 1)(\Gamma_{\rm f} - 1) c^2 \frac{dm_{\rm ext}}{dR_{\rm f}}}^{\text{FS term}} + \overbrace{(\Gamma_{\rm f} - \Gamma_{\rm f0} - \Gamma_{\rm rs,eff} + \Gamma_{\rm rs,eff}\Gamma_{\rm f,rs-rel}) c^2 \frac{dM_{\rm rs,d}}{dR_{\rm f}}}^{\text{RS term}}}{(M_{\rm rs,d} + m_{\rm ext}) c^2 + \mathcal{E}_{\rm ext,in} \frac{d\Gamma_{\rm fs,eff}}{d\Gamma_{\rm f}} + \mathcal{E}_{\rm rs,in} \frac{d\Gamma_{\rm rs,eff}}{d\Gamma_{\rm f}}}, \tag{A5}$$

where the derivatives of $m_{\rm ext}$, $M_{\rm rs,d}$, and $M_{\rm f}$ can be explicitly written as

$$\begin{aligned} \frac{dm_{\rm ext}}{dR_{\rm f}} &= 4\pi R_{\rm f}^2 n_{\rm ext} m_p, \\ \frac{dM_{\rm rs,d}}{dR_{\rm f}} &= \dot{M}_{\rm rs,u} \left(\frac{dR_{\rm f}}{dt}\right)^{-1} \\ &= \frac{3 M_{\rm f} c}{R_{\rm f}} (\beta_{\rm f0} - \beta_{\rm f}) \left(\frac{dR_{\rm f}}{dt}\right)^{-1}, \\ \frac{dM_{\rm f}}{dt} &= \frac{L_{\rm f,iso}}{\Gamma_{\rm f0} c^2} - \frac{3 M_{\rm f} c}{R_{\rm f}} (\beta_{\rm f0} - \beta_{\rm f}). \end{aligned} \tag{A6}$$

In the above expressions, $\beta_{\rm f0} = \sqrt{1 - \Gamma_{\rm f0}^{-2}}$ and $\beta_{\rm f} = \sqrt{1 - \Gamma_{\rm f}^{-2}}$. Equation (A5) is consistent with Equation A1 in Zhang et al. (2023) and it reduces to the simple Equation (9) if

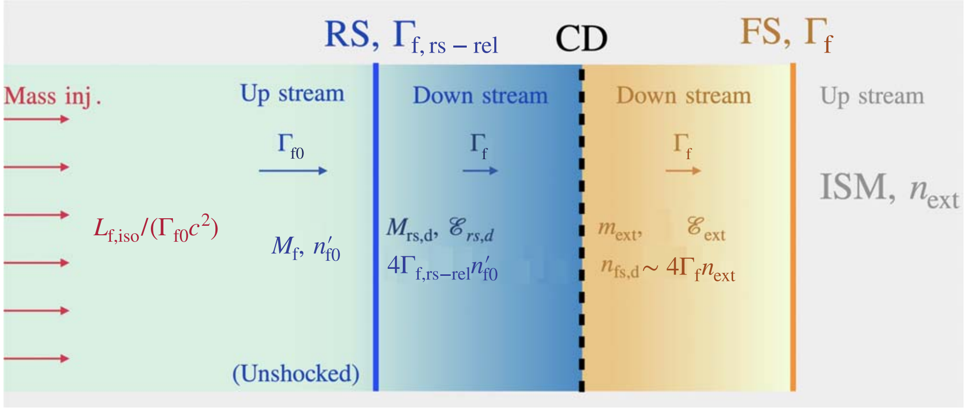

Figure 5. Schematic figure of the fast jet with FS, RS, and continuous energy injection. The contact discontinuity (CD) between the RS and FS downstream is also shown. A detailed description of the physical quantities can be found in the text.

we neglect the influence of the RS by removing the differential terms of RS and letting $M_{\rm rs,d}$ be the ejecta mass $M_{\rm ej}$.

To get an intuition of the dominant factors, we observe that the RS term is a high-order correction in Equation (A5) since $(1-\Gamma_{\rm f}/\Gamma_{\rm f0})\to 0$, $(\Gamma_{\rm f,rs-rel}-1)\to 0$, and $(\beta_{\rm f0}-\beta_{\rm f})\to 0$ when the jet is in the coasting regime. Later, in the deceleration stage we infer the ratio

$$\zeta_{\rm rs/fs} = \frac{\text{RS term}}{\text{FS term}} < \frac{dM_{\rm rs,d}/dR_{\rm f}}{dm_{\rm ext}/dR_{\rm f}} \lesssim \frac{\bar{n}_{\rm rs}}{n_{\rm ext}}\frac{1}{2\Gamma_{\rm f}^2} \lesssim \frac{3\eta_{\rm f}\eta_{\rm acc}M_\star}{16\pi\theta_{\rm f}^2R_{\rm f}^3\Gamma_{\rm f0}\Gamma_{\rm f}^2m_pn_{\rm ext}}, \tag{A7}$$

where $\bar{n}_{\rm rs}\sim M_{\rm f}/(4\pi m_pR_{\rm f}^3/3)$ is the average density of the RS upstream, $M_{\rm f}\lesssim\int L_{\rm f,iso}dt/(\Gamma_{\rm f0}c^2)$, and the definition of $L_{\rm f,iso}$ is used. Plugging in the fiducial values, we find $\zeta_{\rm rs/fs}\lesssim 10^{-2}$ for the fast and slow jet within the data-fitting time window, implying that the RS term in the numerator is negligible. In the denominator, $M_{\rm rs,d}\approx M_{\rm ej}$ (the ejecta mass in Equation (9)) is satisfied as the RS sufficiently crosses and decelerates the ejecta, thus reducing Equation (A5) to Equation (9), and we conclude that the RS does not significantly affect the jet evolution. Our calculation also suggests that the RS term may play a role in the jet evolution when the jet is exceptionally powerful (with higher $\eta_{\rm f}\eta_{\rm acc}M_\star$), extremely narrow (with smaller $\theta_{\rm f}$), and compact (with lower $\Gamma_{\rm f0}$ and $R_{\rm f}$).

Appendix B
Analytical Solutions

Here, we take the fast jet as an example to derive the analytical Lorentz factor evolution, and the lightcurves of the FS and RS scenarios.

B.1. Jet Lorentz Factor

We first derive the fast jet Lorentz factor as a function of $T_{\rm obs}$. Before the fallback time $T_{\rm fb}=(1+z)t_{\rm fb}$, we write down the isotropic-equivalent energy of the jet,

$$\int L_{\rm f,iso}dt \sim \frac{4\pi}{3}R_{\rm f}^2\Gamma_{\rm f}^3n_{\rm ext}m_pc^2. \tag{B1}$$

Noting $R_{\rm f}\sim\Gamma_{\rm f}^2cT_{\rm obs}/(1+z)$, we obtain the time dependence of $\Gamma_{\rm f}$ in the deceleration regime,

$$\Gamma_{\rm f}\propto T_{\rm obs}^{-(2+\alpha)/8},\ \text{for}\ T_{\rm obs}<T_{\rm fb}. \tag{B2}$$

After $T_{\rm fb}$, $L_{\rm f,iso}$ decays faster than t^{-1}, which implies

$$\mathcal{E}_{\rm f,iso}\sim\frac{4\pi}{3}R_{\rm f}^3\Gamma_{\rm f}^2n_{\rm ext}m_pc^2 = \text{const}, \tag{B3}$$

and

$$\Gamma_{\rm f}\propto T_{\rm obs}^{-3/8},\ \text{for}\ T_{\rm obs}>T_{\rm fb}. \tag{B4}$$

The analytical solutions are consistent with Figure 2.

B.2. Fast Jet Forward Shock

Given the parameters in Table 1, the injected electrons are in the fast-cooling regime, i.e., the electron minimum Lorentz factor $\gamma_{e,m}^{\rm fs}$ is larger than the cooling Lorentz factor,

$$\gamma_{e,c}^{\rm fs} = \frac{6\pi m_ec}{(1+Y)\sigma_{\rm T}B_{\rm fs}^2t'_{\rm dyn}}, \tag{B5}$$

where $Y\sim\mathcal{O}(\sqrt{\epsilon_e/\epsilon_B})$ is the Compton parameter (Sari & Esin 2001), $\sigma_{\rm T}$ is the Thomson cross section, and $t'_{\rm dyn}=R_{\rm f}/(\Gamma_{\rm f}c)$ is the comoving dynamic time. We estimate the peak synchrotron flux (e.g., Wijers & Galama 1999),

$$F_{\nu,\rm max}^{\rm (fs)} = \frac{(1+z)f_{\rm br}(0.6f_e^{\rm fs}n_{\rm ext}R_{\rm f}^3)\Gamma_{\rm f}e^3B_{\rm fs}}{\sqrt{3}m_ec^2d_L^2}\sim 9.3 \times 10^{-27}\text{erg s}^{-1}\,\text{cm}^{-2}\,\text{Hz}^{-1}f_{\rm br}\,n_{\rm ext,0.3}^{3/2}\Gamma_{\rm f,0.8}^8(T_{\rm obs}/15\text{days})^3. \tag{B6}$$

In the X-ray bands, e.g., $E_X=10$ keV $=h\nu_X$, we infer the energy flux,

$$\nu F_\nu^{\rm (fs)} = F_{\nu,\rm max}^{\rm (fs)}\nu_c^{1/2}\nu_m^{(s-1)/2}\nu_X^{(1-s/2)} \sim 8.1\times 10^{-14}\text{erg s}^{-1}\,\text{cm}^{-2}, \tag{B7}$$

where $\nu_c = 3\Gamma_{\rm f}(\gamma_{e,c}^{\rm fs})^2eB/[4\pi(1+z)m_ec]$ is the cooling frequency. The analytical value is consistent with the gray dashed curves in Figure 3. Meanwhile, we derive the time dependence of the X-ray emissions produced by the FS,

$$\nu F_\nu^{(\mathrm{fs})}(E_X) \propto \begin{cases} f_{\mathrm{br}}\, T_{\mathrm{obs}}^{-\alpha+1-s/2}, & T_{\mathrm{obs}} < T_{\mathrm{br}} \simeq T_{\mathrm{fb}}, \\ f_{\mathrm{br}}\, T_{\mathrm{obs}}^{-1}, & T_{\mathrm{obs}} > T_{\mathrm{br}} \simeq T_{\mathrm{fb}}, \end{cases} \tag{B8}$$

where $f_{\mathrm{br}} = 1/[1 + (\Gamma_{\mathrm{f}}\theta_{\mathrm{f}})^{-2}]$ is the jet break factor. In our calculation, we infer the jet break time, defined via $\Gamma_{\mathrm{f}}(t_{\mathrm{br}}) = 1/\theta_{\mathrm{f}}$, to be $t_{\mathrm{br}} \simeq 2.8 \times 10^6$ s $\simeq t_{\mathrm{fb}}$, which implies a steepened lightcurve for $T_{\mathrm{obs}} > T_{\mathrm{br}} \simeq T_{\mathrm{fb}}$, $\nu F_\nu^{(\mathrm{fs})}(E_X) \propto \Gamma_{\mathrm{f}}^2 T_{\mathrm{obs}}^{-1} \propto T_{\mathrm{obs}}^{-7/4}$, noting that $\Gamma_{\mathrm{f}} \propto T_{\mathrm{obs}}^{-3/8}$. Equation (B8) indicates that the FS afterglow is disfavored to explain the fast decay of the X-ray lightcurve before and after the fallback time, since it predicts a subdominant slow-decaying X-ray lightcurve.

B.3. Fast Jet Reverse Shock

In the deceleration regime, we have the relative Lorentz factor between the RS up and downstream $\Gamma_{\mathrm{f,\ rs-rel}} = (\Gamma_{\mathrm{f0}}/\Gamma_{\mathrm{f}} + \Gamma_{\mathrm{f}}/\Gamma_{\mathrm{f0}})/2$. The electrons accelerated in the RS region are fast cooling using the parameters in Table 1. Given the accelerated electron number in the RS downstream, $N_{e,\mathrm{rs}} \sim f_e^{\mathrm{rs}}\Gamma_{\mathrm{f,rs-rel}} n_{\mathrm{f0}}{}'(4\pi R_{\mathrm{f}}^2)(R_{\mathrm{f}}/\Gamma_{\mathrm{f}})$, we write down the maximum synchrotron flux at $T_{\mathrm{obs}} = 15$ days,

$$F_{\nu,\max}^{\mathrm{rs}} = \frac{0.6 f_{\mathrm{br}}\sqrt{3}\,(1+z) N_{e,\mathrm{rs}}\Gamma_{\mathrm{f}} e^3 B_{\mathrm{f,rs}}}{4\pi m_e c^2 d_L^2} \simeq 1.2 \times 10^{-26}\mathrm{erg\ s^{-1}\ cm^{-2}\ Hz^{-1}}, \tag{B9}$$

where fiducial values are used to calculate $L_{\mathrm{f,iso}}$, $\Gamma_{\mathrm{f,rs-rel}}$, and $B_{\mathrm{f,rs}}$. From Figure 3, we observe the relationship $\nu_X \gtrsim \nu_m > \nu_c$, where $\nu_m \propto \Gamma_{\mathrm{f}}(\gamma_{e,m}^{\mathrm{rs}})^2 B_{\mathrm{rs}}$ is the characteristic frequency and ν_c is the cooling frequency defined similar to the FS case. In this case, we calculate the X-ray energy flux at $T_{\mathrm{obs}} = 15$ days using the cooling frequency of the RS regime,

$$\nu F_\nu^{(\mathrm{rs})}(E_X) = \nu_c^{1/2}\nu_m^{(s-1)/2}\nu_X^{(1-s/2)}F_{\nu,\max}^{\mathrm{rs}} \sim 1.7 \times 10^{-12}\mathrm{erg\ s^{-1}\ cm^{-2}}. \tag{B10}$$

We also check the time evolution of the X-ray lightcurves,

$$\nu F_\nu^{(\mathrm{rs})}(E_X) \propto \nu_c^{1/2}\nu_m^{(s-1)/2}F_{\nu,\max}^{\mathrm{rs}} \propto \begin{cases} f_{\mathrm{br}}\, T_{\mathrm{obs}}^{-[5\alpha+\alpha(s-1)]/4}, & T_{\mathrm{obs}} < T_{\mathrm{br}} \simeq T_{\mathrm{fb}}, \\ f_{\mathrm{br}}\, T_{\mathrm{obs}}^{-(s+8)/6}, & T_{\mathrm{obs}} > T_{\mathrm{br}} \simeq T_{\mathrm{fb}}. \end{cases} \tag{B11}$$

Similar to the FS case, considering the jet break correction, we obtain a steepened lightcurve for $T_{\mathrm{obs}} > T_{\mathrm{fb}} \simeq T_{\mathrm{br}}$, $\nu F_\nu^{(\mathrm{rs})}(E_X) \propto \Gamma_{\mathrm{f}}^2 T_{\mathrm{obs}}^{-(s+8)/6} \propto T_{\mathrm{obs}}^{-(2s+25)/12} \propto T_{\mathrm{obs}}^{-2.5}$ for $s = 2.3$. Since we adopted the approximations $\Gamma_{\mathrm{f,rs-rel}} \sim \Gamma_{\mathrm{f,\ rs-rel}} - 1 \sim \Gamma_{\mathrm{f0}}/(2\Gamma_{\mathrm{f}})$ to obtain Equation (20), the numerical time decay slope could be steeper by a correction factor $\sim T_{\mathrm{obs}}^{-0.2} - T_{\mathrm{obs}}^{-0.4}$. In this case, the analytical lightcurve aligns well with numerical results depicted in Figure 4 and is in agreement with late-time X-ray upper limits (the red triangles in Figure 4).

ORCID iDs

Chengchao Yuan (袁成超) https://orcid.org/0000-0003-0327-6136
B. Theodore Zhang (张兵) https://orcid.org/0000-0003-2478-333X
Walter Winter https://orcid.org/0000-0001-7062-0289
Kohta Murase https://orcid.org/0000-0002-5358-5642

References

Andreoni, I., Coughlin, M. W., Perley, D. A., et al. 2022, Natur, 612, 430
Barniol Duran, R., Nakar, E., & Piran, T. 2013, ApJ, 772, 78
Berger, E., Zauderer, A., Pooley, G. G., et al. 2012, ApJ, 748, 36
Blandford, R. D., & McKee, C. F. 1976, PhFl, 19, 1130
Bloom, J. S., Giannios, D., Metzger, B. D., et al. 2011, Sci, 333, 203
Brown, G. C., Levan, A. J., Stanway, E. R., et al. 2015, MNRAS, 452, 4297
Burrows, D. N., Kennea, J. A., Ghisellini, G., et al. 2011, Natur, 476, 421
Cendes, Y., Eftekhari, T., Berger, E., & Polisensky, E. 2021, ApJ, 908, 125
Cenko, S. B., Krimm, H. A., Horesh, A., et al. 2012, ApJ, 753, 77
Chevalier, R. A. 1998, ApJ, 499, 810
Crumley, P., Lu, W., Santana, R., et al. 2016, MNRAS, 460, 396
Dai, L., & Fang, K. 2017, MNRAS, 469, 1354
Eftekhari, T., Berger, E., Zauderer, B. A., Margutti, R., & Alexander, K. D. 2018, ApJ, 854, 86
Eftekhari, T., Tchekhovskoy, A., Alexander, K. D., et al. 2024, arXiv:2404.10036
Eichler, D., & Waxman, E. 2005, ApJ, 627, 861
Evans, C. R., & Kochanek, C. S. 1989, ApJL, 346, L13
Genet, F., Daigne, F., & Mochkovitch, R. 2007, MNRAS, 381, 732
Giannios, D., & Metzger, B. D. 2011, MNRAS, 416, 2102
Hayasaki, K. 2021, NatAs, 5, 436
Hills, J. G. 1975, Natur, 254, 295
Huang, Y. F., Dai, Z. G., & Lu, T. 1999, MNRAS, 309, 513
Ioka, K., Kobayashi, S., & Zhang, B. 2005, ApJ, 631, 429
Jiang, N., Zhou, Z., Zhu, J., Wang, Y., & Wang, T. 2023, ApJL, 953, L12
Kippenhahn, R., & Weigert, A. 1990, Stellar Structure and Evolution (New York: Springer)
Klinger, M., Rudolph, A., Rodrigues, X., et al. 2023, arXiv:2312.13371
Liu, D., Pe'er, A., & Loeb, A. 2015, ApJ, 798, 13
Liu, R.-Y., Xi, S.-Q., & Wang, X.-Y. 2020, PhRvD, 102, 083028
Lunardini, C., & Winter, W. 2017, PhRvD, 95, 123001
Matsumoto, T., & Metzger, B. D. 2023, MNRAS, 522, 4028
Metzger, B. D., Giannios, D., & Mimica, P. 2012, MNRAS, 420, 3528
Mimica, P., Giannios, D., Metzger, B. D., & Aloy, M. A. 2015, MNRAS, 450, 2824
Murase, K., Kimura, S. S., Zhang, B. T., Oikonomou, F., & Petropoulou, M. 2020, ApJ, 902, 108
Murase, K., Mészáros, P., & Fox, D. B. 2017, ApJL, 836, L6
Nava, L., Sironi, L., Ghisellini, G., Celotti, A., & Ghirlanda, G. 2013, MNRAS, 433, 2107
Pasham, D. R., Lucchini, M., Laskar, T., et al. 2023, NatAs, 7, 88
Pe'er, A. 2012, ApJL, 752, L8
Phinney, E. S. 1989, in IAU Symp. 136, The Center of the Galaxy, ed. M. Morris (Dordrecht: Kluwer), 543
Piran, T., Svirski, G., Krolik, J., Cheng, R. M., & Shiokawa, H. 2015, ApJ, 806, 164
Rees, M. J. 1988, Natur, 333, 523
Reis, R. C., Miller, J. M., Reynolds, M. T., et al. 2012, Sci, 337, 949
Reusch, S., Stein, R., Kowalski, M., et al. 2022, PhRvL, 128, 221101
Rhodes, L., Bright, J. S., Fender, R., et al. 2023, MNRAS, 521, 389
Rossi, E., Lazzati, D., & Rees, M. J. 2002, MNRAS, 332, 945
Sari, R., & Esin, A. A. 2001, ApJ, 548, 787
Sato, Y., Murase, K., Bhattacharya, M., et al. 2024, PhRvD, 110, L061307
Sato, Y., Obayashi, K., Yamazaki, R., Murase, K., & Ohira, Y. 2021, MNRAS, 504, 5647
Senno, N., Murase, K., & Mészáros, P. 2017, ApJ, 838, 3
Shen, R.-F., & Matzner, C. D. 2014, ApJ, 784, 87
Stein, R., van Velzen, S., Kowalski, M., et al. 2021, NatAs, 5, 510
Teboul, O., & Metzger, B. D. 2023, ApJL, 957, L9
van Velzen, S., Stein, R., Gilfanov, M., et al. 2024, MNRAS, 529, 2559
Wang, J.-Z., Lei, W.-H., Wang, D.-X., et al. 2014, ApJ, 788, 32
Wang, X.-Y., & Liu, R.-Y. 2016, PhRvD, 93, 083005
Wijers, R. A. M. J., & Galama, T. J. 1999, ApJ, 523, 177
Winter, W., & Lunardini, C. 2021, NatAs, 5, 472
Winter, W., & Lunardini, C. 2023, ApJ, 948, 42
Yao, Y., Lu, W., Harrison, F., et al. 2024, ApJ, 965, 39
Yuan, C., Murase, K., Kimura, S. S., & Mészáros, P. 2020, PhRvD, 102, 083013
Yuan, C., Murase, K., Zhang, B. T., Kimura, S. S., & Mészáros, P. 2021, ApJL, 911, L15
Yuan, C., & Winter, W. 2023, ApJ, 956, 30

Yuan, C., Winter, W., & Lunardini, C. 2024, ApJ, 969, 136
Zauderer, B. A., Berger, E., Margutti, R., et al. 2013, ApJ, 767, 152
Zauderer, B. A., Berger, E., Soderberg, A. M., et al. 2011, Natur, 476, 425
Zhang, B. 2018, The Physics of Gamma-ray Bursts (Cambridge: Cambridge Univ. Press)
Zhang, B., & Mészáros, P. 2002, ApJ, 571, 876
Zhang, B. T., Murase, K., Ioka, K., & Zhang, B. 2023, arXiv:2311.13671
Zhang, B. T., Murase, K., Veres, P., & Mészáros, P. 2021, ApJ, 920, 55
Zhou, C., Zhu, Z.-P., Lei, W.-H., et al. 2024, ApJ, 963, 66